Communications Materials

https://doi.org/10.1038/s43246-026-01265-z

Article in Press

Optically anisotropic self-organised ZnO:Al eutectic metamaterial for mid-infrared plasmonics

Received: 18 May 2025

Accepted: 29 June 2026

Published online: 09 July 2026

Cite this article as: Tomczyk, M., Brachaczek, A., Toudert, J. *et al.* Optically anisotropic self-organised ZnO:Al eutectic metamaterial for mid-infrared plasmonics. *Commun Mater* (2026). https://doi.org/10.1038/s43246-026-01265-z

Monika Tomczyk, Aneta Brachaczek, Johann Toudert, Kamil Szlachetko, Barbara Surma, Pawel Osewski, Marcin Gajc, Lars Mester, Gururaj V. Naik, Alexandra Boltasseva, Andrei Bylinkin, Rainer Hillenbrand & Dorota A. Pawlak

Optically anisotropic self-organised ZnO:Al eutectic metamaterial for mid-infrared plasmonics

Monika Tomczyk[1,2#], Aneta Brachaczek[3,4#] Johann Toudert,[1,] Kamil Szlachetko,[2] Barbara Surma,[1] Pawel Osewski,[3] Marcin Gajc,[3] Lars Mester,[5] Gururaj V. Naik,[6,7] Alexandra Boltasseva,[6] Andrei Bylinkin,[5] Rainer Hillenbrand,[8,9,*] Dorota A. Pawlak[1*]

[1]ENSEMBLE[3] Centre of Excellence, Wólczyńska 133, 01-919 Warsaw, Poland

[2]Faculty of Chemistry, University of Warsaw, Pasteura 1, 02-093 Warsaw, Poland

[3]Łukasiewicz Research Network – Institute of Microelectronics and Photonics, Wólczyńska 133, 01-919 Warsaw, Poland

[4]Institute of Fundamental Technological Research, Polish Academy of Sciences, Pawińskiego 5B, 02-106 Warsaw, Poland

[5]CIC nanoGUNE BRTA, Tolosa Hiribidea, 76, E-20018 Donostia – San Sebastian

[6]School of Electrical & Computer Engineering and Birck Nanotechnology Center, Purdue University, 1205 W. State St., West Lafayette, Indiana 47907, USA

[7]Electrical & Computer Engineering, Rice University, 6100 Main St., Houston, Texas 77005, USA

[8]CIC nanoGUNE BRTA and Department of Electricity and Electronics, UPV/EHU, 20018 Donostia-San Sebastián, Spain

[9]IKERBASQUE, Basque Foundation for Science, 48009 Bilbao, Spain

[#] These authors contributed equally to this work

*Corresponding authors. E-mail: dorota.anna.pawlak@ensemble3.eu, r.hillenbrand@nanogune.eu

Abstract

Plasmonic materials have great potential to enable practical applications in the mid-infrared range and would gain in controllability if they were anisotropic. Here, we report an anisotropic mid-infrared plasmonic metamaterial made of less lossy ZnO:Al (AZO) layers embedded in a dielectric $ZnWO_4$ matrix. The described material exhibits a resonance at the 3-4 μm region, which can be switched on/off by changing light polarisation. Polarisation-dependent reflectance spectroscopy, effective medium and finite-difference time-domain modelling demonstrate that the metamaterial exhibits an epsilon-near-zero (ENZ) hybrid photonic-plasmonic resonance, resembling radiative Berreman modes supported by bulk plasmon polaritons in metal thin films. Remarkably, electric field injection into such layers is realised in a simple far-field experiment without prism or focused beams. Importantly, the material is made with the eutectic solidification, which enables achieving AZO layers through self-organization process. Additionally, the widely used crystal growth techniques could enable manufacturing metamaterials on a large scale using the eutectic solidification both in the bulk and thin film form. The methodology can be extended to multiple

material combination and it opens the way to tuneable infrared metamaterials operating at different wavelengths that can find application such as resonant dichroic filters, reflectors, light-trapping structures, and sensors.

1. Introduction

Managing light at mid-infrared (MIR) wavelengths is becoming essential for a wide variety of applications, such as atmospheric and biological sensing, heat transfer, and photothermal conversion[1-3]. This has prompted a growing interest in developing structured material platforms, especially metamaterials, suitable for manipulating MIR light in small dimensions, ideally smaller than the light wavelength.

Metamaterials have gained momentum in relation with plasmonics, which was initially based on the capability of Au or Ag thin films and nanostructured surfaces to support plasmon resonances in the visible wavelength range. The excellent performance in this spectral range can be achieved due to their dielectric function, ε, that displays a slightly negative real part, Re(ε), and a small imaginary part, Im(ε). These specific values of ε enable excitation of surface plasmons that led to effects such as surface-bound electromagnetic wave propagation, subwavelength surface electric field confinement or spatially and spectrally localized optical absorption, which have proven useful for nanophotonic, energy conversion, and sensing applications. More recently, an emphasis was made on metamaterials based on epsilon-near-zero (ENZ) subwavelength structures, for which $\varepsilon \rightarrow 0$, which are especially appealing because they can generate a strong internal electric field under illumination[4] and achieve light tunnelling[5,6], which is ideal for nonlinear optics, nanophotonics, light trapping, and sensing applications[7].

However, usual metamaterials such as those based on Ag or Au do not perform ideally in the MIR range. This is because the dielectric functions of these metals exhibit an excessively high imaginary part ($\mathrm{Im}(\varepsilon) >> 1$, high losses) and an excessively negative real part ($\mathrm{Re}(\varepsilon) << 0$). Thus, alternative materials are needed to build metamaterials harnessing surface plasmons or ENZ condition for the efficient subwavelength manipulation of MIR light[8].

Several candidates have emerged as alternatives to noble metals for plasmonic materials in the near-infrared (NIR) and mid-infrared (MIR) ranges[9]. These include highly doped semiconductors like Al and Ga doped zinc oxide (AZO, GZO[10,11]), indium tin oxide (ITO), transition metal nitrides, silicides, and others[12]. In particular, substituting Zn^{2+} by Al^{3+} and Ga^{3+} ions in ZnO introduces free carriers with doping-dependent concentrations. It was demonstrated that doping ZnO with Al led to plasmonic resonances at 0.61, 1.31, and 1.71 μm wavelength for doping concentrations of 0.8 at.%, 1.6 at.%, and 3.2 at.%, respectively[11]. Therefore, the screened Drude plasma wavelength, at which the material changes its properties from dielectric to metallic, can be adjusted to cover a

broad range of frequencies in these materials[13]. For a properly set carrier concentration (i.e., doping level), in the range of 10^{20} cm^{-3}, this wavelength is located in the MIR region, as predicted by the Drude model[14]. Above this wavelength, the TCO exhibits a metallic behaviour[15], with a moderately negative Re(ε) and a lower Im(ε), lower losses, than that of noble metals. Therefore, these materials can be used for MIR plasmonics, and for achieving MIR epsilon-near-zero properties as well.

Recent studies have brought to light multiple examples of TCO-based metamaterials as well as MIR device concepts based on those materials[16-20]. These studies have shown that special optical effects, such as optical hyperbolism and dichroism, hinge on anisotropic TCO structures. However, many reported implementations use lithography and vacuum deposition techniques, which are costly and suitable for producing only small quantities of materials, in the form of metasurfaces. Consequently, large-scale and low-cost approaches are needed to produce volumetric, anisotropic, TCO-based metamaterials for MIR applications.

In this regard, bottom-up approaches have emerged as effective methods for the fabrication of optical materials over the past years. These approaches include colloidal chemistry[21], electric field-assisted poling[22], anodized alumina-templated assembly of composites[23], metal nanoparticle self-assembly within liquid crystalline phases[24], nanoparticle cluster self-assembly[25-27], template-directed solidification of eutectics[28] and direct doping of dielectric matrices with nanoparticles enabled by the NanoParticle Direct Doping (NPDD)[29-31].

A particularly promising and yet less explored approach exploits the self-organisation mechanism of eutectic solidification. Eutectic composites are two-phase crystalline materials, that simultaneously grow from a homogenous liquid phase at a temperature lower than its original components. These materials can be formed out of various phases and create different geometrical motifs. Their periodic structure refinement can be controlled from the micron scale to the nanoscale by their growth rate. This periodicity is crucial for the formation of photonic bandgaps in photonic crystals or resonant electromagnetic behavior in metamaterials. Recent studies have predicted[32-34] and demonstrated that eutectic composites can behave as photonic crystals when composed of alternating layers, with sub-micron widths and different refractive indices in lamellar structures (of Al_2Cu-Al and AgCl-KCl eutectic)[35], THz metamaterials consisting of LiF rods embedded in either KCl or NaCl[36,37], and visible plasmonic metamaterials utilizing metal-dielectric eutectic system[38,39]. The eutectic composites can form fractal microstructures that in the THz spectral range can act as split-ring resonators[34], eutectic epsilon-near-zero materials[40], waveguides for subwavelength transmission[41], and anisotropic eutectic metamaterials for superlensing[36,37]. On the other hand, in the same eutectic metamaterials formed by Bi_2O_3 and Ag several optical phenomena have been shown. These include tuneable isotropic localised plasmon resonance in the visible range[38,39], nonlinear plasmon-induced optical properties[42], as well as Selective surface-enhanced Raman Scattering in a bulk composite[43]. Therefore, eutectic

solidification presents an unrivalled potential for fabricating a broad variety of self-organised optical metamaterials, in particular anisotropic structures. Furthermore, properly choosing the components and the growth rate can generate the desired optical effects in any spectral regions ranging from visible to THz wavelengths. Therefore, in this paper, we demonstrate the potential of the directional eutectic solidification approach to produce anisotropic TCO-based plasmonic metamaterials for MIR applications.

Eutectic solidification is a well-established industrial process used for large-scale manufacturing of materials with uniform microstructures, including abrasive materials and aluminum alloys for turbine blades and automotive components. Large eutectics, up to 2.4 cm in diameter and 3 cm in length, have been grown via the Czochralski and Bridgman methods[44]. Industrially, the Czochralski crystal growth method can achieve crystal sizes of 300–450 mm in diameter and 1–2 m in length, while the Bridgman method allows for diameters of 10–20 cm and lengths of up to 50 cm, making it suitable for complex compounds. The micro-pulling-down enables smaller, well-shaped eutectics (2–10 mm wide, 30 cm long)[38,45]. Eutectic solidification techniques have also enabled thin-film growth, from early Cd–Zn films with aligned lamellar structures[46] to nanoscale Cu–Ag films (2–400 nm) via co-deposition[47], showing the potential for eutectic structures at various scales.

Although eutectic growth is scalable and cost-effective for fabricating micro- and nanostructures, it requires precise control of thermal gradients and pulling rates to achieve desired phase spacing, which ranges from nanometers to micrometers. Orientation control can be improved using templates, potentially yielding novel structures[48]. Post-processing techniques such as dicing, etching, and integration with lithography, metallization, or passivation can further enhance structural precision and device integration.

Here, we report the fabrication of a volumetric, self-organised nanostructured ZnO:Al–$ZnWO_4$ metamaterial manufactured by directional eutectic solidification. The metamaterial exhibits structural, optical, and plasmonic anisotropy in the MIR range. **Figure 1** shows the growth, structure, and optical properties of the material. The material in form of macroscopic rods is obtained from a melt with a suitable eutectic composition by the one-step micro-pulling-down crystal growth technique (**Figure 1a**). It consists of crystalline ZnO:Al thin layers, with a ~250 nm thickness, placed parallel to each other and usually parallel to the growth direction (**Figure 1b**). The ZnO:Al material shows a negative Re(ε) at MIR wavelengths longer than its screened plasma wavelength, which is located at 3.3 μm (**Figure 1c, top**, measurements done on a bulk ZnO:Al crystal, see **Supporting Information (S1)**). Its Im(ε) is lower than that of Ag in the MIR region. The ZnO:Al layers are embedded in an optically transparent wide-bandgap $ZnWO_4$ crystalline matrix (**Figure 1c, top**). The obtained metamaterial exhibits optical anisotropy at near-normal incidence, when the ZnO:Al layers are oriented perpendicular to the sample surface (**Figure 1c, bottom**). A perpendicularly polarised incident beam (TM-polarised) causes an excited resonance

in the MIR region, which is materialized by a fast increase in the metamaterial's reflectance spectrum as a function of wavelength in the 3-4 μm range (**Figure 1c, bottom**). There is no such increase for a parallel-polarized incident beam (TE-polarised), pointing at the absence of resonance in this case (**Figure 1c, bottom**).

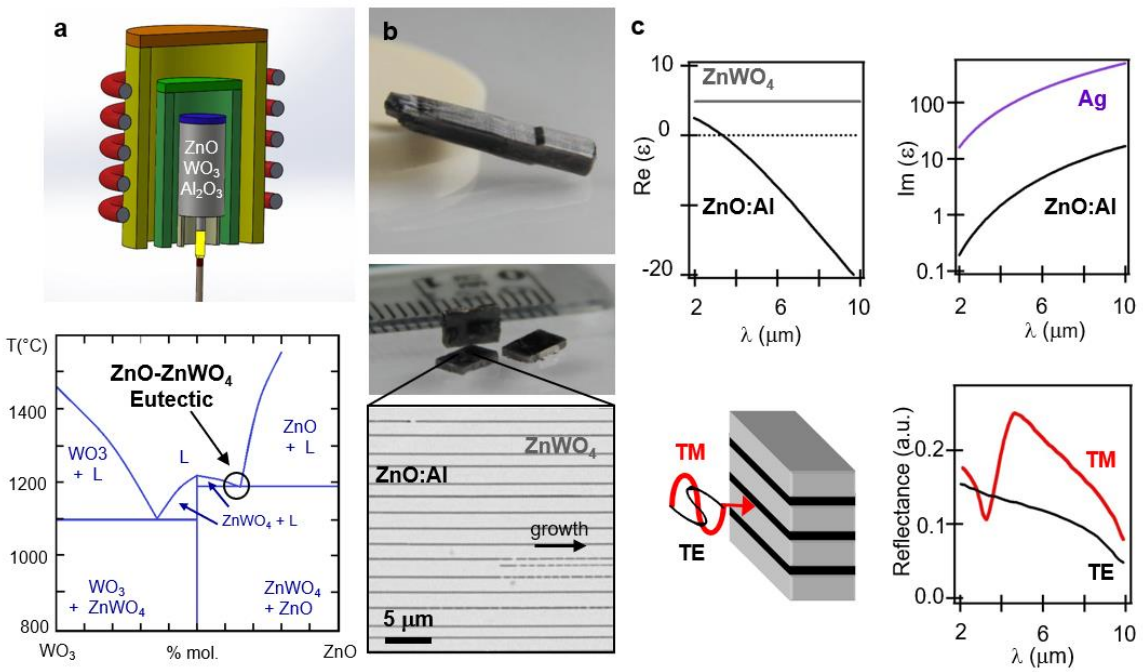

Figure 1. Anisotropic self-organised ZnO:Al-$ZnWO_4$ eutectic metamaterial: fabrication, structure and optical properties. (a) The ZnO:Al-$ZnWO_4$ eutectic metamaterial is produced by introducing ZnO, WO_3, and Al_2O_3 in the micro-pulling-down setup (top panel). ZnO (65 mol.%) and WO_3 compositions (35 mol.%) are chosen to achieve the ZnO-$ZnWO_4$ eutectic point (see phase diagram, bottom panel). (b) Rod-shaped sample manufactured by the micro-pulling-down method (top panel), cut and polished pieces (centre panel), and scanning electron micrograph showing the layered micro/nanostructure (bottom panel), with ZnO:Al layers in dark contrast and the $ZnWO_4$ matrix in bright contrast. (c) MIR dielectric functions ε of ZnO:Al, $ZnWO_4$, and Ag (top panel). Details about the determination of these dielectric functions, done from far-field FTIR reflectance measurements, are given in **Supporting Information (S1)**. The Re(ε) value of ZnO:Al is negative for $\lambda > 3.3$ μm, while its Im(ε) is much smaller than for Ag (lower losses). $ZnWO_4$ is a transparent dielectric (Re(ε) > 0, Im(ε) = 0). The measured MIR reflectance spectra of the metamaterial for TE- and TM-polarised incident light (bottom panel) demonstrating its optical anisotropy and a resonant character for TM-polarised light. The data shown in this figure are those of materials in which ZnO was nominally doped with 10 at.% Al.

It will be shown later that, at this resonance, an epsilon-near-zero plasmonic mode develops with the electric field enhanced inside the subwavelength-thick (<λ/10) ZnO:Al layers. Such enhanced electric field is achieved with no need of optics to couple the incident collimated light. This contrasts with metallic (Ag, Au) and dielectric (Si_3N_4, Al_2O_3) waveguides, where launching an optical mode requires special coupling set-ups such as a prism or focusing optics[49]. Such direct coupling is ascribed to the Berreman-like nature of the excited mode. Berreman modes are bulk excitations that were first reported in very thin polaritonic films in spectral regions where $\varepsilon \rightarrow 0$.

In contrast with bulk plasmons that are longitudinal waves, and therefore cannot interact with the transverse free-space light, Berreman modes are not solely longitudinal. Thus, they can be excited by free-space light and radiate part of the electromagnetic power they absorb.

In the metamaterial considered here, each ZnO:Al layer efficiently interacts with the incident light because of the Berreman-like nature of the excited mode. The interaction of light with the ZnO:Al-$ZnWO_4$ metamaterial is further enhanced due to the presence of many layers, so that the light that is radiated or diffracted by each of them can be coupled into the others. This property can be especially useful for manufacturing tuneable and wavelength-selective resonant dichroic filters, reflectors, and light-trapping structures for the MIR range, as well as environmental sensors[50].

2. Results and discussion

Fabrication, structure and composition of the anisotropic volumetric layered ZnO:Al–$ZnWO_4$ eutectic

To demonstrate the effectiveness of eutectic solidification for manufacturing plasmonic MIR metamaterials, we manufactured a eutectic mixture with a ZnO phase. The ZnO-WO_3 system enabled the formation of ZnO layers embedded in a $ZnWO_4$ matrix, a eutectic consisting of 65 mol% ZnO and 35 mol% WO_3[51] consistent with our previous findings[52,53]. ZnO is a semiconductor (E_g=3.1–3.3 eV) that decomposes easily even at lower temperatures despite its high melting point (1975 °C), which makes it difficult to obtain from a melt. On the other hand, $ZnWO_4$ is a wide-bandgap dielectric (E_g=4–5 eV) that is transparent in a broad wavelength range (from ~320 nm to ~10 μm). A eutectic mixture exhibits a lower melting temperature than that of its original components. This is why our composite presents a lower melting temperature (1187 °C) than that of ZnO, which allows ZnO to grow from the melt without decomposition[51].

To increase the free carrier concentration of ZnO above 10^{18} cm^{-3} (the value for intrinsic ZnO), the composite was doped with Al^{3+} ions at different nominal concentrations (0, 1, 5, 10 at.%). The eutectic composites were grown into few-centimetre-long rods with a rectangular cross-section (3 mm × 5 mm) using the micro-pulling-down technique. Doping with Al changed the colour of the obtained composites: the undoped material was light beige (**Figure 2a**), while the doped materials were dark grey (**Figure 2b,c**).

The Al-doped ZnO-$ZnWO_4$ eutectic crystallized in the broken lamellar micro/nanostructure (**Figure 2d**), similar to the undoped eutectic[52,53]. The broken lamellar nanostructure features a small volume ratio of the lamellar/layered phase to the matrix phase and holes in the lamellae/layers filled with the matrix phase[53]. The layers are oriented almost along the growth direction of the rod-shaped samples. As mentioned above, the layered and matrix phases predominantly consist of ZnO and $ZnWO_4$, respectively. Similar diffraction peaks were observed

in the X-ray powder diffractograms for all samples (see an example of such diffractogram in **Figure 2e**). On the other hand, energy dispersive spectroscopy showed that Al^{3+} concentrations amounted to ~0.3 and ~0.1 at.% in ZnO and $ZnWO_4$, respectively, indicating that a small amount of Al^{3+} ions was incorporated into both phases (see **Figure 2f**). This results from the low solubility of Al in ZnO, which is below 0.003 at.%[54]. The excess dopant has formed a new phase, $ZnAl_2O_4$, detected by micro-Raman measurements (see Supporting information and **Figure S4.1**).

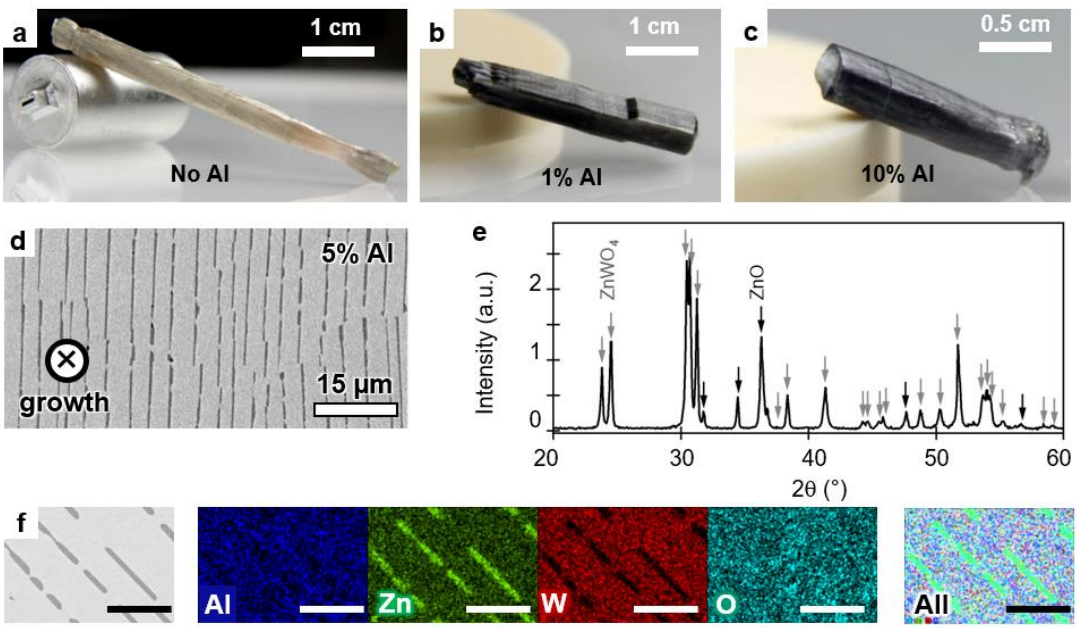

Figure 2. Structure and composition of the anisotropic ZnO:Al-$ZnWO_4$ metamaterial doped with different Al concentrations. Examples of manufactured ZnO-$ZnWO_4$ rods: (a) undoped and doped with (b) 1 at.% Al, and (c) 10 at.% Al. (d) Scanning electron micrograph showing the micro/nanostructure of ZnO:Al-$ZnWO_4$ (5 at.%). (e) X-ray powder diffraction of ZnO:Al-$ZnWO_4$ (10 at.%) indicating the presence of $ZnWO_4$ (grey arrows) and ZnO (black arrows) in the eutectic. (f) Energy dispersive spectroscopy of ZnO:Al-$ZnWO_4$ revealing the distribution of different elements in the material.

Local optical properties of the ZnO:Al layers and $ZnWO_4$ matrix

We used s-SNOM to verify that the dielectric function of the lamellae is the same as that of the bulk material. In particular, we observe a transition of the real part of the permittivity from negative to positive around a wavelength of 3 µm. This demonstrates that, during the eutectic growth process, the carrier concentration in the lamellae remains similar to the original bulk material. In contrast, far-field measurements of the lamellar sample are diffraction-limited and probe large sample areas that include many lamellae of both constituent materials. As a result, the ENZ behavior can only be inferred indirectly through modeling of the measured spectra. To this end, a ZnO:Al-$ZnWO_4$ material doped with 10% Al was cut perpendicularly to the growth direction, allowing for Atomic Force Microscopy (AFM) imaging of an individual ZnO:Al layer embedded in the $ZnWO_4$ matrix (**Figure 3a**). A series of five s-SNOM amplitude s_3 and phase φ_3 images was

recorded using illumination wavelengths λ from 2.8 µm to 3.2 µm (exemplary shown for λ = 2.9 µm in **Figure 3d,f** and for λ = 3.2 µm in **Figure 3e,g**). Signals were normalized to the average near-field signal of the dielectric $ZnWO_4$ matrix, for which we assume a spectrally independent permittivity ε_{ZnWO4} = 4.84 in the MIR range.[55] The small s-SNOM amplitude s_3 contrast observed in **Figure 3d** indicates a small near-field reflectivity of ZnO:Al at λ = 2.9 µm (dielectric). Interestingly, s_3 is strongly increased on the ZnO:Al layer at λ = 3.2 µm (**Figure 3e**), which is indicative of a high near-field reflectivity (metallic). A large s-SNOM phase φ_3 contrast is observed at λ = 2.9 µm, which reduces slightly at λ = 3.2 µm, **Figure 3f,g**.

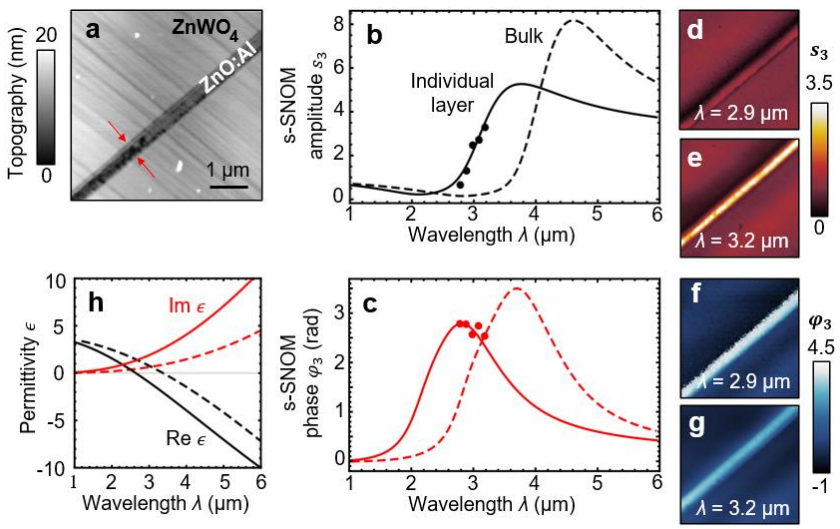

Figure 3. Plasmonic behavior of ZnO:Al layers near epsilon-near-zero wavelength studied by s-SNOM. (a) Topography map. s-SNOM data was analysed in the area marked by arrows. (b) s-SNOM amplitude s_3 and (c) phase φ_3 spectra obtained experimentally (symbols) and calculated for an individual ZnO:Al layer (solid curves; N and τ were fit parameters) and bulk ZnO:Al (dashed curves; N and τ were determined by far-field FTIR reflectance, see **Supporting Information (S1)**). s-SNOM signals are normalized to that of the $ZnWO_4$ matrix. (d,e) Exemplary s_3 and (f,g) φ_3 images corresponding to panels a-c. (h) Real part (black) and imaginary part (red) of the ZnO:Al permittivity ε, determined by far-field FTIR reflectance (dashed curves) and by s-SNOM (solid curves).

To quantify the optical properties of the ZnO:Al layer, **Figures 3b,c** show s_3 and φ_3 as a function of λ (contrasts were evaluated at the position marked by arrows in **Figure 3a**). For comparison, we calculated s-SNOM spectra using a monopole model,[56] for a semi-infinite sample of permittivity $\varepsilon = \varepsilon_\infty - Ne^2/[\varepsilon_0 m^* m_0 (\omega^2 + i\omega/\tau)]$ at frequencies $\omega = 2\pi c/\lambda$, where N and m^* are the free carrier concentration and effective mass, τ is their collision time, ε_∞ is the high-frequency permittivity of the sample, ε_0 is the vacuum permittivity, c the speed of light, e the elementary charge and m_0 the electron mass (solid lines in **Figure 3b,c**). We find excellent agreement between experimental and calculated data for $N = 2.8 \cdot 10^{20}$ cm^{-3} and τ = 4.0 fs, while keeping m^* = 0.4 and ε_∞ = 3.88 at the values found for the bulk crystal of ZnO:Al (**Supporting Information (S1)**). **Figure 3h** shows the corresponding ε obtained on the 500-nm thick ZnO:Al layer (solid lines), yielding a screened plasma wavelength of $\lambda_p \approx 2.6$ µm and losses that are significantly lower than

that of Ag in the MIR range. We note that for the individual ZnO:Al layer the plasma wavelength is blue-shifted when compared to the bulk ZnO:Al crystal ($\lambda_p \approx 3.3$ µm), owing to the slightly increased N (from $N = 1.6 \cdot 10^{20}$ cm^{-3}) and the decreased τ (from $\tau = 7.8$ fs). However, near-field measurements also have limitations. While far-field spectra probe a large sample volume and provide a statistical average over many ZnO:Al lamellae embedded in the transparent $ZnWO_4$ matrix, s-SNOM probes only a very shallow surface region and extracts the dielectric function from a single lamella. Since aluminum incorporation can vary with factors such as layer thickness, crystallographic orientation, and local temperature gradients during growth, local s-SNOM results and statistical far-field measurements may differ. Both methods, therefore, provide complementary information about the material. To better visualize the spectral shift of λ_p, dashed lines in **Figures 3b,c,h** show the expected values for bulk ZnO:Al.

Summarizing, the fitting and extrapolation of s-SNOM data indicate that the screened plasma wavelength of the ZnO:Al layer is located in the MIR region. This indicates that such a layer should display a plasmonic character at MIR wavelengths above this screened plasma wavelength. These effects are enabled by a suitable free carrier concentration in ZnO. From the analysis of complementary UV-Vis far-field optical absorption measurements, it is proposed that such free carriers are brought by Al^{3+} doping. Indeed, such measurements indicated that doping the composite with Al^{3+} ions caused a blueshift of the ZnO absorption edge from ~383 to 369 nm (3.23–3.36 eV) (**Figure 4a** (top)). This is consistent with the Burstein-Moss effect, which manifests itself as an increase in the apparent band gap of the semiconductor when states close to and at the bottom of the conduction band become populated[57]. Doping affected the absorption edge of the $ZnWO_4$ phase to a lesser extent. This suggests that the presence of Al in $ZnWO_4$ does not introduce a significant number of free carriers in this material. Therefore, we refer to ZnO:Al layers and a $ZnWO_4$ matrix to describe these phases in this manuscript.

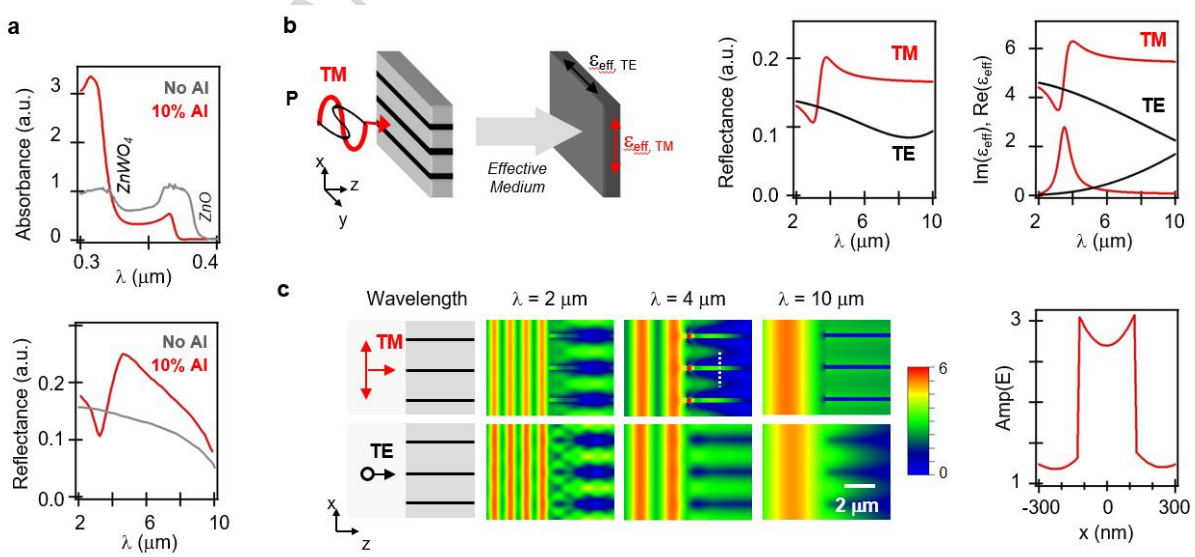

Figure 4. Exploration of the polarization-dependent optical resonance observed in the ZnO:Al-$ZnWO_4$ eutectic metamaterial: spectral and electromagnetic field analysis. (a) Properties of undoped and Al-doped ZnO-$ZnWO_4$ (10 at.% Al). The UV absorbance spectra show a blueshift of the ZnO bandgap upon doping (top panel). The MIR

reflectance spectra, measured with TM-polarised light, display a fast reflectance increase with wavelength in the 3–4 μm region that is only present in the Al-doped metamaterial (bottom panel). (b) Effective medium simulations of the dielectric function and reflectance of a metamaterial consisting of ZnO:Al layers (volume fraction 10%) in a $ZnWO_4$ matrix. The effective medium shows different reflectance signatures with TE- and TM-polarised light, which originate from different dielectric functions along ($\varepsilon_{eff,TE}$) and perpendicularly to the layers ($\varepsilon_{eff,TM}$). With TM-polarised light, a resonance is observed near 3.5 μm. This resonance leads to the fast reflectance increase observed in the reflectance spectrum. (c) FDTD maps of the electric field amplitude, at different incident wavelengths for a ZnO:Al-$ZnWO_4$ metamaterial with 250 nm-thick ZnO:Al layers and a 2 μm periodicity. The color bar represents the ratio $|E|/|E_0|$, of the computed complex electric field and the incident complex electric field in air. For TM-polarised light at a wavelength of 4 μm, the electric field is enhanced inside the ZnO:Al layers, with a hotspot at their edge. At $\lambda = 4$ μm the dotted vertical line in these layers indicates the field profile, which resembles that of a Berreman mode.

Analysis of the anisotropic optically resonant MIR response of the metamaterial: Effective medium modeling

Because of their layered anisotropic nanostructure, the ZnO:Al-$ZnWO_4$ metamaterials exhibited optical anisotropy and especially polarisation-dependent resonant behaviour in the MIR range. This effect was observed experimentally when the ZnO:Al-$ZnWO_4$ cross section, cut perpendicularly to the crystal growth direction, was exposed to infrared light at near-normal incidence. The reflectance measurements of material cross sections exposed to light polarised perpendicularly to the layers (TM-polarised) showed a fast increase as a function of wavelength in the 3-4 μm (**Figure 1c, bottom**; **Figure 4a, bottom**). No such increase occurred when the incident light was polarised parallel to the layers (TE-polarisation, **Figure 1c, bottom**). In that case, the reflectance slowly decreased with increasing wavelength. In contrast, the undoped material did not show any reflectance increase vs wavelength under TM-polarised illumination (**Figure 4a, bottom**), suggesting that the anisotropic resonant behaviour is specific to the doped composite.

To account for this polarisation-dependent resonant behaviour and elucidate its origin, the reflectance of the material was first evaluated through simple effective medium calculations, assuming a perfect ZnO:Al-$ZnWO_4$ layered structure. These simulations required the dielectric functions of ZnO:Al and $ZnWO_4$. For ZnO:Al (**Figure 1c, top**), the bulk dielectric function of this material was used. As explained before and shown in **Figure 3h**, this function was successfully modelled by a Drude function with a screened plasma wavelength $\lambda_p \approx 3.3$ μm, demonstrating that ZnO:Al nanostructures are suitable for supporting plasmonic effects ($Re(\varepsilon)<0$) in the MIR range. The dielectric function of $ZnWO_4$ (**Figure 1c, top**) was positive and almost wavelength independent in the MIR region. Further details about the dielectric properties of these materials are given in **Supporting Information (S1)**. Information about the effective medium calculations is given in **Supporting Information (S2)**.

In qualitative agreement with the experimental spectra, the simulated TM-polarised reflectance (**Figure 4b**) displayed a fast increase as a function of wavelength with an inflexion point at a

wavelength of approximately 3.5 μm, and this increase was not observed under TE-polarised light. To understand the origin of this increase and its occurrence only in specific polarisation conditions, we also determined the corresponding simulated effective dielectric function of the layered material (**Figure 4b)**. Under TM polarisation, the increase was clear in the $Re(\varepsilon_{eff})$ spectrum and was correlated to a peak in the $Im(\varepsilon_{eff})$ spectrum. This peak indicates a resonant optical absorption in the spatially confined ZnO:Al layers in the presence of a perpendicularly oriented electric field. Under TE-polarisation, the $Re(\varepsilon_{eff})$ function continuously decreased with increasing wavelength while the $Im(\varepsilon_{eff})$ function increased. This suggests that no excited resonance occurred in the MIR region with this polarisation but that the ZnO:Al layers behave as an (infinite) optically metallic material.

Hybrid photonic – epsilon-near-zero plasmonic resonance explored via FDTD calculations

To explore the nature and features of the resonance observed under exposure to TM-polarised light, we assessed the electromagnetic field in the ZnO:Al-$ZnWO_4$ metamaterial through Finite-Difference Time-Domain (FDTD) calculations. The calculations are detailed in the **Supporting Information (S3, Figure S3.1)**. The thickness of the ZnO:Al layers was set to 250 nm in the calculations to achieve consistency with the scanning electron microscopy, (SEM) observations. The obtained field maps for TM-polarised light **(Figure 4c)** showed that, in the wavelength range of the resonance (see field map at $\lambda = 4$ μm), the electric field was enhanced inside the ZnO:Al layers and displayed a nearly flat transverse profile. In this wavelength region, the $Re(\varepsilon)$ of ZnO:Al is negative but close to 0. This implies that the resonance has an epsilon-near-zero plasmonic origin.

Furthermore, the type of profile observed resembles that of the radiative Berreman modes of polaritonic thin films[7,8,58]. These modes were first observed in thin films with markedly subwavelength thickness, at the vicinity of vibrational bands where $Re(\varepsilon) \rightarrow 0$. However, similar modes can be excited regardless of the origin of the near cancellation of $Re(\varepsilon)$, for instance, at the vicinity of the screened Drude plasma wavelength of metals or other conductors. In this work, the ZnO:Al thickness (250 nm) is 16 times smaller than the wavelength (4 μm). This value is inside the range of thickness-to-wavelength ratios for which radiative Berreman modes were reported. The advantage of this structure over others is that the enhanced electric field in the ZnO:Al layers is generated directly from the incident collimated light. This means that no special coupling strategies, such as using a grating or a prism, are required (see **Figure 4c**). Nonetheless, the enhanced electric field inside the layers reached a depth nearing 2 μm. To achieve a greater field enhancement depth, reducing $Im(\varepsilon_{eff})$ would be required. Therefore, the advantage of these structures, due to the intrinsic losses of ZnO:Al, does not lie in field enhancement effects but in their ability to absorb light.

Additional FDTD simulations were performed on a single ZnO:Al layer embedded in $ZnWO_4$ to further explore the features of such an enhanced field (**Supporting Information S3, Figure S3.2**). These simulations revealed that the enhanced electric field could be achieved already in a single layer. The field amplitude would become higher in a thinner ZnO:Al layer, as shown in **Figure S3.2**, and in the literature for AlN films[59]. However, in the actual multi-layered metamaterial, light propagating in the $ZnWO_4$ matrix also couples with the ZnO:Al layers. Therefore, in this metamaterial, the enhanced field in the ZnO:Al layers likely results from a combination of direct incoupling and indirect coupling of the light propagating in the $ZnWO_4$ matrix. Thus, for the sake of correctness, the mode excited in the metamaterial should be named the "hybrid photonic–epsilon-near-zero plasmonic mode". The spectral and spatial features of this mode are expected to depend on the metamaterial structure, including the thickness of different layers. Indeed, we have observed that its spectral position depends on the microstructure refinement. For thicker ZnO:Al layers and larger distances between them, the resonance becomes redshifted and less pronounced (**Figure 5**). In addition, because Al has a low solubility limit in ZnO and its incorporation depends on the segregation coefficient, the Al concentration within the ZnO lamellas can vary along the eutectic rod. This variation alters the free-carrier density in the ZnO:Al and, consequently, the ZnO:Al plasma frequency. As a result, the spectral position of the resonance can shift accordingly.

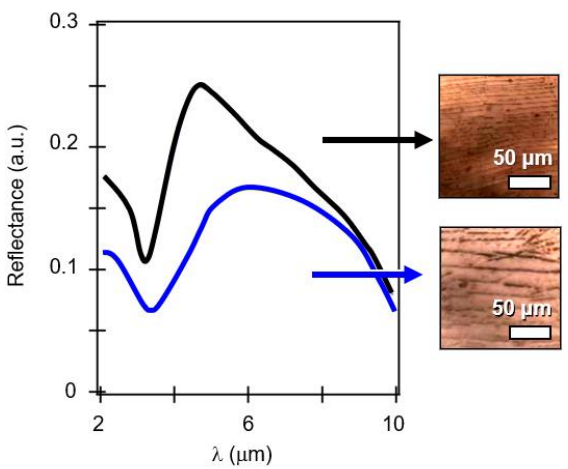

Figure 5. ZnO:Al-$ZnWO_4$ eutectic metamaterial micro/nanostructure dependent MIR optical response. The two curves represent the reflectance spectra with TM-polarized light of ZnO:Al-$ZnWO_4$ metamaterials doped with the same amount of Al, but presenting different micro/nanostructures (ZnO:Al layers thickness and periodicity).

4. Conclusions

We have manufactured self-organised ZnO:Al-$ZnWO_4$ metamaterials with a layered nanostructure by directional eutectic solidification, a simple crystal growth method. The metamaterials exhibit

optical anisotropy in the MIR range. This anisotropy, which translates into dichroism, is related to the excitation of an hybrid photonic – epsilon-near-zero plasmonic resonance when the incident light is polarised perpendicularly to the ZnO:Al layers. The dichroism achieved by selective control of the linear polarization of the incident light can be utilized to achieve switchability of the optical response of the metamaterial, and thus selective control of the reflectance. This is the first demonstration of such an effect in the MIR region for a eutectic metamaterial. Furthermore, the observed hybrid photonic – epsilon-near-zero plasmonic resonance can be tailored by varying the metamaterial nanostructure and composition.

These structural and optical properties make the fabricated metamaterial an interesting candidate for applications requiring tuneable resonances in the MIR range. The most straightforward applications are wavelength-selective dichroic filters and reflectors as well as MIR light trapping structures. In addition, a matrix presenting an environment-dependent refractive index can enable sensing applications by utilizing refractive index matching condition. Furthermore, the developed metamaterial can simultaneously selectively filter or reflect MIR light and conduct electricity because of the percolated structure of the ZnO:Al layers. With the fabricated metamaterial, dynamic polarisation control of the MIR light could be achieved. In many materials, the optical properties can be tuned by changing the refractive indices of component phases. In the case of the presented metamaterial, the piezoelectric effect of ZnO:Al plates could be used for changing their refractive index by applying an electric field. This would enable tuning the spectral position of the resonance in a wavelength range. The tuneability of optical properties has already been shown in the pure ZnO-$ZnWO_4$ eutectic metamaterial when changing the temperature and shifting anomalous optical transmission near 397 nm[52].

In contrast with top-down fabrication methods, the bottom-up manufacturing process, reported here, is a flexible approach to preparing volumetric layered materials. Directional eutectic solidification presents a cost-effective and rapid alternative to traditional top-down nanofabrication methods like Electron Beam Lithography (EBL). While EBL achieves high nanoscale precision below 10 nm, it has disadvantages such as low throughput and high costs due to its serial writing process, which can take hours per wafer[60]. In contrast, eutectic solidification is a self-assembly process where structures form spontaneously from the melt, growing at speeds of up to ~20 mm/min.

Moreover, the materials can be cut in an arbitrary way, thus enabling a deliberate layer orientation with respect to the incident beam. In this work, the hybrid photonic – epsilon-near-zero plasmonic resonance is excited with the incident light parallel to the ZnO:Al layers. To the best of our knowledge, this is the first demonstration of this excitation geometry for epsilon-near-zero structures. This approach enables an enhanced electric field inside these layers without the need for a coupling device. This finding suggests that suitably fabricated eutectic metamaterials can be used for the free-space coupling of light to nano-waveguides. Furthermore, if the incident light

was parallel to the layers in a conventional configuration, hyperbolic properties could be achieved upon proper material design (**Supporting Information (S4)**).

This study focused on the ZnO:Al-$ZnWO_4$ composite but a multitude of eutectic composites and a plethora of available compounds, such as oxides[61], metals, semiconductors, insulators, thermoelectric[62], ferroelectric, or ferromagnetic materials or even organic compounds[63], could be used as components. Despite limited general knowledge in this area, eutectic composites play an important role in many everyday life applications ranging from inks for printers to liquid crystal displays.

Regular eutectic micro/nanostructures exhibiting layered or rod-like geometry can be utilised as photonic materials. In most cases, precipitate size and interprecipitate distance can be controlled with the growth rate, providing readily tuneable properties and wavelength of interest and, as a consequence, leading to tailored plasmonic elements[64] or modulators[65]. Recent studies have demonstrated that eutectic layered composites can grow into circular forms[66,67], which could lead to applications such as the hyperlens[68]. They also can be grown in templates resulting in Archimedean structures enabling manufacturing of metasurfaces or materials with improved mechanical properties[28]. Eutectics can also be used to manufacture flexible metamaterials[69] that can be directly written as mesoscale architectures[70]. Additionally, such ordered micro/nanocomposite structures can be obtained not only via eutectic transition (1 liquid → 2 solids) but also via spinodal decomposition (1 solid → 2 solids)[71].

Thus, further developments of novel crystal-growth based composites, such as eutectics, spinodal composites, can enable on-demand development of materials with multiple functionalities, available at different wavelength ranges, with tuneable properties, and where a slight change of the composition (as doping) or a structure can lead to new functionality.

5. Methods

Crystal growth

The ZnO-WO_3 system presents two eutectic points and zinc oxide is one of the component phases at the eutectic composition of 65 mol.% ZnO and 35 mol.% WO_3. The melting temperature at the chosen eutectic point approximates 1187 °C, which is much lower than that of pure zinc oxide (1975 °C), and at this condition, the material does not decompose rapidly. High-purity oxide powders ZnO (99.999%), WO_3 (99.98%), and Al_2O_3 (99.999%) by Alfa Aesar were used as starting materials. The oxides were mixed with isopropanol in an agate mortar and then dried at 130 °C. Four different material compositions were prepared: pure and Al^{3+}-doped ZnO-$ZnWO_4$ eutectic (1, 5, and 10 at.%).

The eutectic composites were grown by the micro-pulling-down method, in which the raw materials are melted in an iridium crucible with a die at the bottom in which a centrally placed nozzle is located. The melt that exudes from the nozzle contacts a seed crystal to continuously crystallise while being pulled down. The crystal is pulled down as it forms. The material was seed grown from a $SrLaGaO_4$ crystal in nitrogen atmosphere. The iridium crucible consisted of a rectangular shaper (3 mm × 5 mm) and a slit (1 mm × 3 mm). The synthesized rods were sectioned into 1-2 mm slices, which were subsequently polished down to a thickness of 100-1000 μm for further characterization. The surface scratches visible on the samples result from the mechanical polishing process used to prepare them for AFM/s-SNOM measurements.

Microstructure and phase characterisation

Microstructures were characterised using a Carl Zeiss scanning electron microscope (SEM) Auriga® CrossBeam® Workstation at the Łukasiewicz Research Network – Institute of Microelectronics and Photonics (Ł-IMIF) equipped with an energy dispersive spectroscopy detector for chemical composition analysis. X-ray powder diffraction measurements were performed on a Siemens D500 diffractometer equipped with a Si:Li detector and Kα Cu (λ = 1.5418 Å) radiation.

Optical characterisation

Transmittance measurements in the ultraviolet–visible range were performed using a CRAIC 20/20 PV microspectrophotometer fitted with Carl Zeiss quartz optical components and an integrated imaging system with Xe illumination source. The transmitted signal was acquired by 10× objective and 11 × 11 μm aperture and detected by a CCD matrix (1024 × 58 pixels) in spectral range of 200–1000 nm with a spectral resolution of 0.45 nm.

Reflectance measurements in the infrared range were carried out by Fourier spectrophotometer (VERTEX 80v, Bruker). The broadband thermal source was a Nernst glower polarised in perpendicular (P-polarisation) and parallel (S-polarisation) to the ZnO:Al layers and acquired by a Mercury Cadmium Telluride (MCT) detector in a range of 8000 – 400 cm^{-1}.

Scattering-type Scanning Near-Field Optical Microscopy (s-SNOM) measurements were performed using a commercially available s-SNOM setup (neaSNOM by neaspec GmbH), combined with standard PtIr5-coated AFM tips (ARROW-NCPt, NanoWorld, tip radius 25 nm) and a monochromatic IR laser light source (Compact OPO VIS by Coherent), which is pumped by a Ti:Sa laser (Chameleon Ultra by Coherent). The IR laser radiation (power set to 2 mW) is focused onto the AFM tip, which acts as an optical antenna,[72] effectively concentrating the IR radiation into an electromagnetic hot spot below the tip apex and yielding a spatial resolution of approximately $\lambda/100$. The tip-scattered light is detected by a liquid nitrogen-cooled MCT detector

in an asymmetric Michelson interferometer setup, yielding IR amplitude and phase spectra[73]. The relation between incident electric field, E_{in}, and the near-field scattered by the tip, E_{sca}, can be expressed as: $E_{sca} = \sigma E_{in}$, where amplitude s and phase φ of the scattering coefficient $\sigma = se^{i\varphi}$ essentially describe the near-field reflection and near-field absorption of the sample. To separate the near-field signals from unwanted far-field components, the AFM is operated in tapping-mode (tip tapping amplitude 50 nm and tapping frequency $\Omega \approx 250$ kHz) and the detector signal is demodulated at the 3rd higher harmonic of the tapping frequency Ω[74].

Calculated s-SNOM contrasts were obtained using a monopole model[67], in which the AFM-tip is approximated as a prolate spheroid with an apex radius 25 nm and a major half-axis length 300 nm. Near-fields created by an electric monopole near the tip apex are reflected at the sample surface and act back onto the tip, inducing an additional charge distribution into the tip. The model parameter $g = 0.7e^{0.06i}$ describes which part of the induced charge is relevant for the near-field interaction[75]. In our calculations, we use a tapping amplitude $A = 50$ nm, corresponding to the experimental value.

Acknowledgements

MT, KS, and BS thank the TEAM Project (POIR.04.04.00-00-3DBE/16-01) of the Foundation for Polish Science, co-financed by the European Union under the European Regional Development Fund. DAP is grateful for the „Centre of ExcelleNce for nanophotonicS, advancEd Materials and novel crystal growth-Based technoLogiEs - ENSEMBLE3" project which is carried out within the 2.1 International Research Agendas programme of the Foundation for Polish Science co-financed by the European Union under the European Funds for Smart Economy 2021-2027 (FENG) and the European Union Horizon 2020 research and innovation program Teaming for Excellence (GA. No. 857543) for supporting this work. The publication was created as part of the project of the Minister of Science and Higher Education, "Support for the activities of Centers of Excellence established in Poland under the Horizon 2020 program" under contract No. MEiN/2023/DIR/3797. AB acknowledges support from the Office of Naval Research (ONR) of the United States Department of Defense under award ONR MURI #N00014-10-1-0942.

Funding Declaration

The author(s) disclosed receipt of the following financial support for the research, authorship, and/or publication of this article: TEAM Project (POIR.04.04.00-00-3DBE/16-01) of the Foundation for Polish Science, co-financed by the European Union under the European Regional Development Fund; „Centre of ExcelleNce for nanophotonicS, advancEd Materials and novel crystal growth-Based technoLogiEs - ENSEMBLE3" project which is carried out within the 2.1

International Research Agendas programme of the Foundation for Polish Science co-financed by the European Union under the European Funds for Smart Economy 2021-2027 (FENG) and the European Union Horizon 2020 research and innovation program Teaming for Excellence (GA. No. 857543); Minister of Science and Higher Education, "Support for the activities of Centers of Excellence established in Poland under the Horizon 2020 program" under contract No. MEiN/2023/DIR/3797; Office of Naval Research (ONR) of the United States Department of Defense under award ONR MURI #N00014-10-1-0942.

Declaration of competing interests

The authors declare no competing interests.

Author Contributions

MT, AA, KS, BS, PO, and MG performed the experiments and analyzed the data; JT, KS, ABy, and LM performed the theoretical calculations; AA, PO, and MG grew the eutectic composites; MT, AA, and KS wrote and revised the manuscript; GN and ABo provided critical commentary on TCO; RH and DAP coordinated the work; DAP conceived the idea. All co-authors revised the manuscript before submission.

Data availability

The data supporting the conclusions are reported in this study and are available upon request from the corresponding author.

References

1. Li, Y. *et al.* Transforming heat transfer with thermal metamaterials and devices. *Nature Reviews Materials* **6**, 1–20 (2021).
2. Rodrigo, D. *et al.* Mid-infrared plasmonic biosensing with graphene. *Science* **349**, 165–168 (2015).
3. Herminjard, S. *et al.* Surface Plasmon Resonance sensor showing enhanced sensitivity for CO_2 detection in the mid-infrared range. *Opt. Express* **17**, 293–303 (2009).
4. Shaykhutdinov, T., Furchner, A., Rappich, J. & Hinrichs, K. Mid-infrared nanospectroscopy of Berreman mode and epsilon-near-zero local field confinement in thin films. *Opt. Mater. Express* **7**, 3706–3714 (2017).
5. Campione, S., Brener, I. & Marquier, F. Theory of epsilon-near-zero modes in ultrathin films. *Phys. Rev. B - Condens. Matter Mater. Phys.* **91**, 1–5 (2015).
6. Silveirinha, M. & Engheta, N. Tunneling of electromagnetic energy through subwavelength channels and bends using ε-near-zero materials. *Phys. Rev. Lett.* **97**, 1–4 (2006).
7. Alù, A. & Engheta, N. Dielectric sensing in -near-zero narrow waveguide channels. *Phys. Rev. B - Condens. Matter Mater. Phys.* **78**, 1–5 (2008).
8. Maas, R., Parsons, J., Engheta, N. & Polman, A. Experimental realization of an epsilon-near-zero metamaterial at visible wavelengths. *Nat. Photonics* **7**, 907–912 (2013).
9. Stanley, R. Plasmonics in the mid-infrared. *Nat. Photonics* **6**, 409-411 (2012).

10. Kapetanovic, V., Bicket, I. C., Lazar, S., Lagos, M. J. & Botton, G. A. Tunable Infrared Plasmon Response of Lithographic Sn-doped Indium Oxide Nanostructures. *Adv. Opt. Mater.* **8**, 1–8 (2020).
11. Calzolari, A., Ruini, A. & Catellani, A. Transparent Conductive Oxides as Near-IR Plasmonic Materials: The Case of Al-Doped ZnO Derivatives. *ACS Photonics* **1**, 703–709 (2014).
12. Darabian R. *et.al.* Compendium of Natural Epsilon-Near-Zero Materials, *ACS Photonics* **12**, 3042-3052 (2025**)**.
13. Buonsanti, R., Llordes, A., Aloni, S., Helms, B. A. & Milliron, D. J. Tunable infrared absorption and visible transparency of colloidal aluminum-doped zinc oxide nanocrystals. *Nano Lett.* **11**, 4706–4710 (2011).
14. Drude, P. Zur Elektronentheorie der Metalle. *Ann. Phys.,* **306**, 566-613 (1900).
15. Kim, J., Naik, G. V., Emani, N. K., Guler, U. & Boltasseva, A. Plasmonic resonances in nanostructured transparent conducting oxide films. *IEEE J. Sel. Top. Quantum Electron.* **19**, (2013).
16. Papadakis, G. T. & Atwater, H. A. Field-effect induced tunability in hyperbolic metamaterials. *Phys. Rev. B - Condens. Matter Mater. Phys.* **92**, 1–11 (2015).
17. Naik, G. V., Liu, J., Kildishev, A. V., Shalaev, V. M. & Boltasseva, A. Demonstration of Al:ZnO as a plasmonic component for near-infrared metamaterials. *Proc. Natl. Acad. Sci. U. S. A.* **109**, 8834–8838 (2012).
18. Kalusniak, S., Orphal, L. & Sadofev, S. Demonstration of hyperbolic metamaterials at telecommunication wavelength using Ga-doped ZnO. *Opt. Express* **23**, 32555 (2015).
19. Huang, Y. W. *et al.* Gate-Tunable Conducting Oxide Metasurfaces. *Nano Lett.* **16**, 5319–5325 (2016).
20. Alam, M. Z., De Leon, I. & Boyd, R. W. Large optical nonlinearity of indium tin oxide in its epsilon-near-zero region. *Science (80-.).* **352**, 795–797 (2016).
21. Li, J., Hill, E. H., Lin, L. & Zheng, Y. Optical Nanoprinting of Colloidal Particles and Functional Structures. *ACS Nano* **13**, 3783–3795 (2019).
22. Beresna, M. *et al.* Poling-assisted fabrication of plasmonic nanocomposite devices in glass. *Adv. Mater.* **22**, 4368–4372 (2010).
23. Wen, L., Xu, R., Mi, Y. & Lei, Y. Multiple nanostructures based on anodized aluminium oxide templates. *Nat. Nanotechnol.* **12**, 244–250 (2017).
24. Wojcik, M. *et al.* Liquid-crystalline phases made of gold nanoparticles. *Angew. Chemie - Int. Ed.* **48**, 5167–5169 (2009).
25. Mühlig, S. *et al.* Optical properties of a fabricated self-assembled bottom-up bulk metamaterial. *Opt. Express* **19**, 9607 (2011).
26. Tan, S. J., Campolongo, M. J., Luo, D. & Cheng, W. Building plasmonic nanostructures with DNA. *Nat. Nanotechnol.* **6**, 268–276 (2011).
27. Fan, J. A. *et al.* Self-assembled plasmonic nanoparticle clusters. *Opt. InfoBase Conf. Pap.* **328**, 1135–1139 (2010).
28. Kulkarni, A. A., Hanson, E., Zhang, R., Thornton, K. & Braun, P. V. Archimedean lattices emerge in template-directed eutectic solidification. *Nature* **577**, 355–358 (2020).
29. Gajc, M. *et al.* Nanoparticle direct doping: Novel method for manufacturing three-dimensional bulk plasmonic nanocomposites. *Adv. Funct. Mater.* **23**, 3443–3451 (2013).
30. Nowaczynski, R. *et al.* Manufacturing of Volumetric Glass–Based Composites with Single- and Double-QD Doping. *Part. Part. Syst. Charact.* **36**, 1–6 (2019).
31. Gajc, M., Surma, H. B. & Pawlak, D. A. Optically-active metastable defects in volumetric

nanoplasmonic composites. *Sci. Rep.* **8**, 1–10 (2018).
32. Pawlak, D. A. *et al.* Second order self-organized pattern of terbium-scandium-aluminum garnet and terbium-scandium perovskite eutectic. *J. Appl. Phys.* **91**, 9731–9736 (2002).
33. Pawlak, D. A. *et al* Self-Organized, Rodlike, Micrometer-Scale Microstructure of $Tb_3Sc_2Al_3O_{12}$−$TbScO_3$:Pr Eutectic. *Chem. Mater.* **18**, 2450–2457 (2006).
34. Pawlak, D. A. *et al.* How far are we from making metamaterials by self-organization? the microstructure of highly anisotropic particles with an SRR-like geometry. *Adv. Funct. Mater.* **20**, 1116–1124 (2010).
35. Kim, J. *et al.* Template-Directed Directionally Solidified 3D Mesostructured AgCl-KCl Eutectic Photonic Crystals. *Adv. Mater.* **27**, 4551–4559 (2015).
36. Basharin, A. A., Kafesaki, M., Economou, E. N. & Soukoulis, C. M. Superlensing effects in anisotropic eutectic metamaterials in the THz range. *AIP Conf. Proc.* **1398**, 64–66 (2011).
37. Reyes-Coronado, A. *et al.* Self-organization approach for THz polaritonic metamaterials. *Opt. Express* **20**, 14663 (2012).
38. Sadecka, K. *et al.* When eutectics meet plasmonics: Nanoplasmonic, volumetric, self-organized, silver-based eutectic. *Adv. Opt. Mater.* **3**, 381–389 (2015).
39. Sadecka, K., Toudert, J., Surma, H. B. & Pawlak, D. A. Temperature and atmosphere tunability of the nanoplasmonic resonance of a volumetric eutectic-based Bi_2O_3-Ag metamaterial. *Opt. Express* **23**, 19098 (2015).
40. Massaouti, M. *et al.* Eutectic epsilon-near-zero metamaterial terahertz waveguides. *Opt. Lett.* **38**, 1140 (2013).
41. Myroshnychenko, V. *et al.* Interacting plasmon and phonon polaritons in aligned nano- and microwires. *Opt. Express* **20**, 10879 (2012).
42. Deska, R. *et al.* Nonlinear plasmonics in eutectic composites: Second harmonic generation and two-photon luminescence in a volumetric Bi_2O_3-Ag metamaterial. *Appl. Phys. Lett.* **110**, 1–5 (2017).
43. Szlachetko, K. *et al.* Selective surface-enhanced Raman scattering in a bulk nanoplasmonic Bi_2O_3-Ag eutectic composite. *Nanophotonics* **9**, 4307–4314 (2020).
44. Yui Takizawa, Y. *et al.* Large size growth of terbium doped $BaCl_2$/NaCl/KCl eutectic for radiation imaging. *Jpn. J. Appl. Phys.* **61,** SC1009 (2022).
45. Bienkowski, K. *et al.* Growth of a Plate-Shaped $SrTiO_3$–TiO_2 Eutectic. *Crystal Growth & Design* **11**, 3935-3940 (2011).
46. Albers, W. *et al.* Aligned eutectic thin film growth. *J. Cryst. Growth* **18**, 147-150 (1973).
47. Misják, F. Growth of nanocomposite in eutectic Cu–Ag films. *Thin Solid Films* **518,** 4247-4251 (2010).
48. Kulkarni, A. A. *et al.* Template-Directed Solidification of Eutectic Optical Materials**.** *Adv. Opt. Mater.* **6**, 1800071, (2018).
49. Newman, W. D. *et al.* Ferrell-berreman modes in plasmonic epsilon-near-zero media. *ACS Photonics* **2**, 2–7 (2015).
50. Fusco, Z. *et al.* Non-periodic epsilon-near-zero metamaterials at visible wavelengths for efficient non-resonant optical sensing. *Nano Lett.* **20**, 3970–3977 (2020).
51. Shchenev, A., Kargin, Y. & Skorikov, M. The ZnO–WO_3 system. *Russ J Inorg Chem* **33**, 2165–2167 (1988).
52. Osewski, P. *et al.* New Self-Organization Route to Tunable Narrowband Optical Filters and Polarizers Demonstrated with ZnO–$ZnWO_4$ Eutectic Composite. *Adv. Opt. Mater.* **8**, 1–10 (2020).

53. Tomczyk, M. *et al.* Bulk nanocomposite made of ZnO lamellae embedded in the $ZnWO_4$ matrix: growth from the melt. *J. Mater. Sci.* **56**, 11219–11228 (2021).
54. Serier, H., Gaudon, M. & Ménétrier, M. Al-doped ZnO powdered materials: Al solubility limit and IR absorption properties. *Solid State Sci.* **11**, 1192–1197 (2009).
55. Yang, F. & Tu, C. The spectroscopy investigation of $ZnWO_4$:Tm^{3+} single crystal. *J. Alloys Compd.* **535**, 83–86 (2012).
56. Cvitkovic, A., Ocelic, N. & Hillenbrand, R. Analytical model for quantitative prediction of material contrasts in scattering-type near-field optical microscopy, *Opt. Express* **15**, 8850-8565 (2007).
57. Grundmann, M. *The Physics of Semiconductors*. Springer International Publishing (2016).
58. Berreman, D. W. Infrared Absorption at Longitudinal Optic Fretluency in Cubic Crystal Films. *Phys. Rev.* **130**, 2193–2198 (1963).
59. Nordin, L. *et al.* Mid-infrared epsilon-near-zero modes in ultra-thin phononic films. *Appl. Phys. Lett.* **111**, 091105, (2017).
60. Basu P. *et al.* Advancements in lithography techniques and emerging molecular strategies for nanostructure fabrication. *Int.J.Mol. Sci.* **26**, 3027 (2025).
61. Waku, Y. *et al.* A ductile ceramic eutectic composite with high strength at 1,873 K. *Nature* **389**, 49–52 (1997).
62. Beretta, D. *et al.* Thermoelectrics: From history, a window to the future. *Mater. Sci. Eng. R Reports* **138**, 210–255 (2019).
63. Simon, F. *et al.* Enhanced second harmonic generation from an organic self-assembled eutectic binary mixture: A case study with 3-nitrobenzoic and 3,5-dinitrobenzoic acids. *Cryst. Growth Des.* **15**, 946–960 (2015).
64. Naik, G. V., Shalaev, V. M. & Boltasseva, A. Alternative plasmonic materials: Beyond gold and silver. *Adv. Mater.* **25**, 3264–3294 (2013).
65. Babicheva, V. E. *et al.* Towards CMOS-compatible nanophotonics: Ultra-compact modulators using alternative plasmonic materials. *Opt. Express* **21**, 27326 (2013).
66. Urbas, A. M. *et al.* Roadmap on optical metamaterials. *Journal of Optics (United Kingdom)* vol. 18 093005 (2016).
67. Akamatsu, S., Bottin-Rousseau, S., Şerefoğlu, M. & Faivre, G. Lamellar eutectic growth with anisotropic interphase boundaries: Experimental study using the rotating directional solidification method. *Acta Mater.* **60**, 3206–3214 (2012).
68. Liu, Z., Lee, H., Xiong, Y., Sun, C. & Zhang, X. Far-field optical hyperlens magnifying sub-diffraction-limited objects. *Science* **315**, 1686 (2007).
69. Acosta, M. F., Rodrigo, S. G., Martín-Moreno, L., Pecharromán, C. & Merino, R. I. Micropillar Templates for Dielectric Filled Metal Arrays and Flexible Metamaterials. *Adv. Opt. Mater.* **5**, 1–6 (2017).
70. Boley, J. W. *et al.* High-Operating-Temperature Direct Ink Writing of Mesoscale Eutectic Architectures. *Adv. Mater.* **29**, (2017).
71. Chen, Z. *et al.* Self-Assembled, Nanostructured, Tunable Metamaterials via Spinodal Decomposition. *ACS Nano* **10**, 10237–10244 (2016).
72. Novotny, L. & Hecht, B. *Principles of Nano-Optics*, 1st edition, Cambridge (2006).
73. Ocelic, N., Huber, A., Hillenbrand, R., Pseudoheterodyne detection for background-free near-field spectroscopy, *Appl. Phys. Lett.* **89**, 101124 (2006).
74. Kurihara, T., Yamaguchi, K., Watanabe, H., Nakajima, M. & Suemoto, T. Dielectric probe for scattering-type terahertz scanning near-field optical microscopy, *Appl. Phys. Lett.* **103**, 151105

(2013).
75. Cvitovic, A., Ocelic, N. & Hillenbrand, R., Analytical model for quantitative prediction of material contrasts in scattering-type near-field optical microscopy, *Opt. Express* **15**, 14, 8850-8565 (2007).